

Strong spin depolarization in the ferromagnetic Weyl semimetal $\text{Co}_3\text{Sn}_2\text{S}_2$: Role of spin-orbit coupling

Sandeep Howlader,¹ Surabhi Saha,² Ritesh Kumar,¹ Vipin Nagpal,³ Satyabrata Patnaik,³ Tanmoy Das,² and Goutam Sheet^{1,*}

¹*Department of Physical Sciences, Indian Institute of Science Education and Research Mohali, Mohali, Punjab, India*

²*Department of Physics, Indian Institute of Science, Bengaluru, Karnataka, India*

³*School of Physical Sciences, Jawaharlal Nehru University, Delhi, India*



(Received 17 June 2019; accepted 8 September 2020; published 30 September 2020)

$\text{Co}_3\text{Sn}_2\text{S}_2$ has recently emerged as a ferromagnetic Weyl semimetal. Theoretical investigation of the spin-split bands predicted half metallicity in the compound. Here, we report the detection of a spin-polarized supercurrent through a Nb/ $\text{Co}_3\text{Sn}_2\text{S}_2$ point contact where Andreev reflection is seen to be large, indicating a large deviation from half metallicity. In fact, analysis of the Andreev reflection spectra reveals very small spin polarization at different points with the degree of spin polarization ranging from 20% to 50% at the Fermi level of $\text{Co}_3\text{Sn}_2\text{S}_2$. Our theoretical calculations of electronic density of states reveal a spin-depolarizing effect near the Fermi energy when the role of spin-orbit coupling is included. The inclusion of spin-orbit coupling also reveals particle-hole asymmetry that explains a large asymmetry observed in our experimental Andreev reflection spectra.

DOI: [10.1103/PhysRevB.102.104434](https://doi.org/10.1103/PhysRevB.102.104434)

I. INTRODUCTION

$\text{Co}_3\text{Sn}_2\text{S}_2$ has recently attracted significant attention due to the presence of a unique ferromagnetic Weyl semimetallic phase [1,2] with possible half metallicity in the compound. The ferromagnetic phase was experimentally measured to appear below 177 K. The band-structure calculations on $\text{Co}_3\text{Sn}_2\text{S}_2$ reveal the existence of ferromagnetic order along with a band gap for spin minority band at the Fermi level [3]. Support for half metallicity was also obtained from angle-resolved and core-level photo-emission spectroscopy [4] on $\text{Co}_3\text{Sn}_2\text{S}_2$. Recently, the compound has come under notice again because several experiments indicated a novel topological Weyl phase in $\text{Co}_3\text{Sn}_2\text{S}_2$. In this context, a large intrinsic anomalous Hall effect [2] was measured in crystals of $\text{Co}_3\text{Sn}_2\text{S}_2$, where the Weyl fermions provided a dominant contribution to the Hall conductivity. Details of the topological surface Fermi arc states were investigated theoretically [5] in $\text{Co}_3\text{Sn}_2\text{S}_2$. A giant anomalous Nernst signal [6], much larger than the known ferromagnets, was obtained on the material where it was argued that the enhanced contribution was due to a Berry curvature [7,8] close to the Fermi level. The unique combination of topological Weyl behavior and high spin-polarization may open up new areas of Weyl spintronics. Therefore, investigation of the spin-resolved transport properties of the Fermi surface of $\text{Co}_3\text{Sn}_2\text{S}_2$ is of utmost importance. While the spin polarization of the spin-split bands of the system was earlier investigated by photoemission spectroscopy, the transport spin polarization of the Fermi surface remains an outstanding problem.

In this paper, we report on the measurement of transport spin polarization in $\text{Co}_3\text{Sn}_2\text{S}_2$ by spin-resolved point contact Andreev reflection (PCAR) spectroscopy [9–14]. Our

measurements show that, contrary to the expectation within band-structure calculations, the transport spin polarization in $\text{Co}_3\text{Sn}_2\text{S}_2$ is $\sim 50\%$, not 100%. A detailed analysis of the experimental data and our calculations, including the role of spin-orbit coupling in the compound, reveal a prominent spin-depolarization effect near the Fermi energy driven by spin-orbit coupling, and thus the significantly reduced transport spin polarization is explained.

II. EXPERIMENTAL DETAILS & THEORETICAL BACKGROUND

High-quality single crystals of $\text{Co}_3\text{Sn}_2\text{S}_2$ were used for the low-temperature experiments presented here. $\text{Co}_3\text{Sn}_2\text{S}_2$ single crystals were synthesized using the modified Bridgman method [4,15,16]. The crystal structure and phase of the single crystals were determined from the Reitveld refinement of powder x-ray diffraction. The refinement confirms the trigonal crystal structure with spacegroup $R\bar{3}m(166)$. The derived lattice parameters are $a = 5.3686 \text{ \AA}$ and $c = 13.1747 \text{ \AA}$. The resistivity measurement of $\text{Co}_3\text{Sn}_2\text{S}_2$ revealed metallic behavior in the entire temperature range with a small kink observed at 177 K signaling a magnetic transition. The resistivity $\rho(2\text{K})$ is found to be $14 \mu\Omega\text{-cm}$ with $\text{RRR} = 35$, which implies the good quality of our crystals. Next, we performed a temperature-dependent measurement of magnetization M with $H = 500 \text{ G}$. Transition to the ferromagnetic phase is again confirmed from the measurement. The derivative of magnetization shows the sharp magnetic transition around 177 K.

All the measurements were done in a liquid helium cryostat equipped with a superconducting vector magnet ($6T-1T-1T$) [16]. For temperature-dependent experiments, a variable temperature insert (VTI) was used, which operates between 1.4 and 300 K. The point-contact spectroscopy [17–19] experiments were performed using a home-built probe based on the

*goutam@iisermohali.ac.in

standard needle-anvil method. The surface of the crystals were polished prior to the point-contact spectroscopy experiments. The point contacts were formed *in situ* at low temperatures. We carefully chose the ballistic point contacts for analysis and data where critical current-dominated artifacts were identified and rejected. The electronic transport through a ballistic point-contact between a normal metal and a conventional superconductor is dominated by a quantum process called Andreev reflection that involves the reflection of a spin-up (down) electron as a spin-down (up) hole from the interface. Andreev reflection leads to a special kind of nonlinearity in the I - V spectrum, which is directly probed in a dI/dV versus V spectrum recorded across such a point contact. The Andreev reflection spectra are traditionally analyzed by a model developed by Blonder, Tinkham, and Klapwijk (BTK) [20,21]. The model assumes a δ -function potential barrier whose strength is characterized by a dimensionless parameter Z which is proportional to the strength of the barrier at the interface. Ideally, for elemental superconductors where the quasiparticle life-time (usually represented by Γ) is very small, the Andreev reflection spectra can be fitted using two fitting parameters, Z and Δ , the superconducting energy gap. For all nonzero values of Z , a dI/dV spectrum shows a double-peak structure symmetric about $V = 0$ —this is a hallmark of Andreev reflection.

When the metal in the metal-superconductor point-contact is a ferromagnet with finite spin polarization at the Fermi level, the density of states of the up-spin electrons [$N_{\uparrow}(E_F)$] is not equal to the density of states of the spin-down electrons [$N_{\downarrow}(E_F)$]. Therefore, $|N_{\uparrow}(E_F) - N_{\downarrow}(E_F)|$ electrons encountering the interface cannot undergo Andreev reflection because they do not find accessible states in the opposite spin band. Therefore, in a point-contact between a ferromagnetic conductor and a conventional superconductor, Andreev reflection is suppressed. Clearly, for a half-metallic ferromagnet, the Andreev reflection is expected to be completely suppressed leading to zero conductance below $V = \pm\Delta/e$, and no features associated with Andreev reflection should appear in a dI/dV versus V spectrum. For nonhalf metals, by measuring the degree of the suppression of Andreev reflection, the spin-polarization of the Fermi level can be measured. To extract the absolute value of the Fermi level spin polarization, first the BTK current is calculated for zero spin polarization ($I_{\text{BTK}u}$) and 100% spin polarization ($I_{\text{BTK}p}$), respectively. Then the current for an intermediate spin polarization P_t is calculated by interpolation between ($I_{\text{BTK}u}$) and ($I_{\text{BTK}p}$) following the relation $I_{\text{total}} = I_{\text{BTK}u}(1 - P_t) + P_t I_{\text{BTK}p}$. The derivative of I_{total} with respect to V gives the modified Andreev reflection spectrum with finite spin polarization in the nonsuperconducting electrode forming the point contact [22]. This model is traditionally used to analyze the spin-polarized Andreev reflection spectra obtained between a ferromagnetic metal and a superconductor by using four fitting parameters Z , Δ , Γ , and P_t . It is to be noted that for a mesoscopic transport experiment, one measures the transport spin polarization (P_t), which depends on the spin-dependent Fermi velocities of the electrons. The transport spin polarization is given by $P_t = \frac{\langle N_{\uparrow} v_{F\uparrow}^n \rangle - \langle N_{\downarrow} v_{F\downarrow}^n \rangle}{\langle N_{\uparrow} v_{F\uparrow}^n \rangle + \langle N_{\downarrow} v_{F\downarrow}^n \rangle}$, where $n = 1, 2$ for ballistic and diffusive regimes, respectively [23].

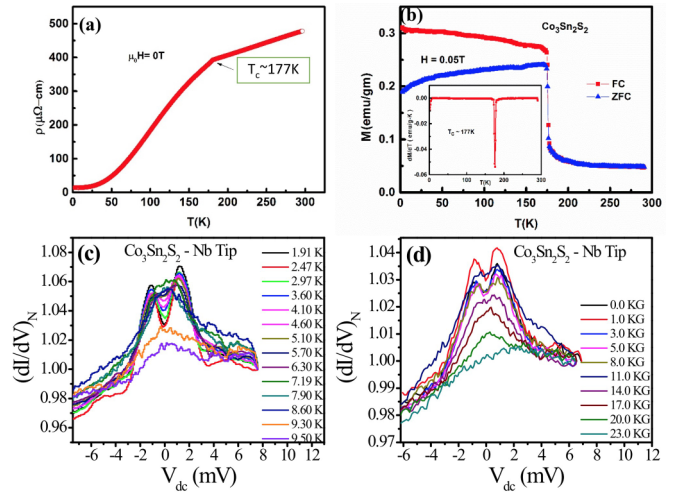


FIG. 1. (a) Resistivity versus temperature plot showing ferromagnetic to paramagnetic transition at Curie temperature $T_c = 177$ K. (b) Variation of magnetization with temperature showing field cool and zero field cool curves. (c) Temperature-dependent asymmetric PCAR spectra. (d) Magnetic-field-dependent asymmetric PCAR spectra. The point contact resistance R_{PC} is 0.88Ω .

III. RESULTS & DISCUSSIONS

In Fig. 1, we show a number of differential conductance (dI/dV) spectra obtained for a point contact between $\text{Co}_3\text{Sn}_2\text{S}_2$ and a sharp tip of the conventional superconductor Nb at varying temperatures [Fig. 1(c)] and magnetic fields Fig. 1(d) [16]. The two peaks in conductance around $V = 0$ are the peaks due to Andreev reflection. This is surprising since $\text{Co}_3\text{Sn}_2\text{S}_2$ is known to be a half metallic ferromagnet for which Andreev reflection must be completely suppressed. To note, the conductance at zero-bias is large, confirming substantial Andreev reflection occurring at $\text{Co}_3\text{Sn}_2\text{S}_2/\text{Nb}$ interfaces. The spectra systematically evolve with temperature and all the features associated with Andreev reflection disappear around 9 K, the critical temperature of Nb. Similarly the features gradually disappear with increasing magnetic field, as expected.

One may, in principle, argue that the suppression could be due to certain defect-induced inelastic processes going on under the point contacts [24,25]. However, the clear observation of Andreev-reflection-dominated features guarantee that the contacts are in the ballistic (or diffusive) regime and definitely not in the thermal regime where the inelastic scattering leads to contact heating. In the thermal regime, contact heating also causes conductance dips in the spectra due to the dominant contribution of the critical current-dominated I - V characteristics of the superconducting electrode. As can be seen in the presented data, our spectra are free from such artifacts.

One important feature of all the spectra is an asymmetry about $V = 0$. This asymmetry is always seen for this system. Above the critical temperature and magnetic field, where the spectral features disappear, the asymmetry persists. As we will show later, this asymmetry stems from an asymmetry in the density of states when spin-orbit coupling is included in the calculation. While in this case, we found an understanding of the asymmetry from the band structure, other sources of asymmetry like a local thermoelectric emf generation cannot

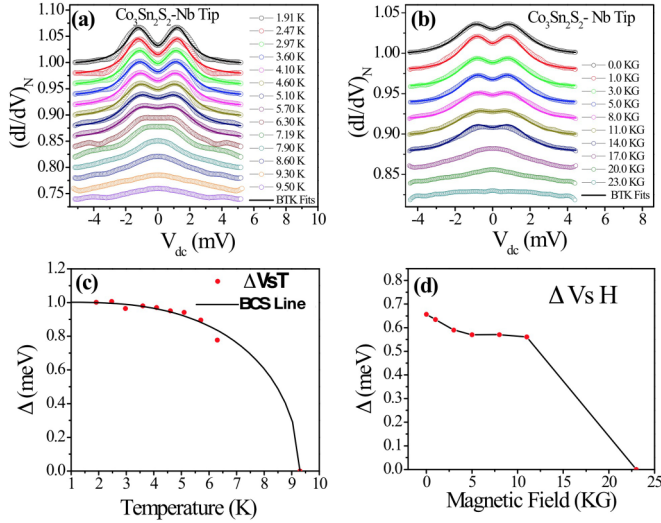


FIG. 2. (a) Temperature dependence of conductance spectra with corresponding BTK fits. (b) Magnetic field dependence of conductance spectra with corresponding BTK fits. (c) Δ versus T with BCS Line. (d) Δ versus H .

be totally ruled out. However, the asymmetry in this system is surprisingly large and persistent. For the analysis of spin polarization within the modified BTK model, we extracted the symmetric component of spectra [26]. We showed the temperature [Fig. 2(a)] and magnetic field [Fig. 2(b)] evolution of the point contact spectra [16]. The data obtained for each temperature and magnetic field are normalized to the conductance at the highest voltage bias (the normal state). The colored points show the (symmetrized) experimental data points and the solid lines show the theoretical fits within the modified BTK model as discussed above (also see sSupplemental Material). The measured superconducting energy gap (Δ) is found to be 1 meV, which is smaller than the gap of pristine Nb. This reduction in Δ of Nb can be attributed to the proximity of the ferromagnetic $\text{Co}_3\text{Sn}_2\text{S}_2$. However, the reduced gap evolves with temperature following the prediction within BCS theory [27,28] [Fig. 2(c)]. Hence, the presence of the Weyl semimetal did not cause a deviation from the conventional nature of superconductivity. Δ also decreases gradually with increasing magnetic field [Fig. 2(d)]. The fittings presented here also provide a quantitative estimate of the intrinsic ($Z = 0$) transport spin polarization. To find this quantity, we first captured a number of spectra with varying Z and analyzed them. The extracted values of P_i from such analysis were plotted as a function of Z . The extrapolation of that to $Z = 0$ gives the intrinsic P_i [29]. The intrinsic P_i thus measured is found to be $\sim 50\%$ at lowest temperature and zero magnetic field. For the fittings up to 9 K, P_i was kept constant at its low-temperature value. The distribution of P_i that were used for this analysis is shown in a pie chart [Fig. 3(b)]. As it is seen, for none of the point contacts does the spin polarization approach 100%.

The presence of spin-polarized current in the point contacts is further confirmed by the field angle dependence of resistance of a ballistic point contact. We rotated the magnetic field using a 3-axis vector magnet with respect to the direction of the applied current. The data for $V = 0$ is pre-

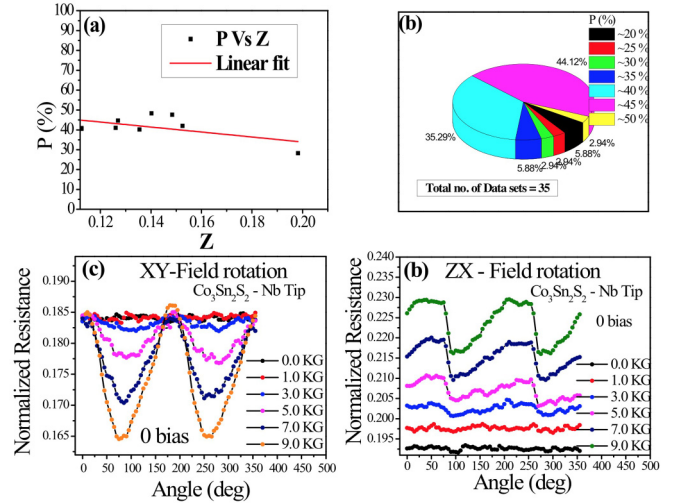


FIG. 3. (a) Spin polarization (P) versus barrier strength (Z) plot. Extrapolation to $Z = 0$ is represented by the solid line where spin polarization approaches 45%. (b) Statistics of spin polarization obtained for different point contacts. (c), (d) Angular magnetoresistance performed at zero voltage bias and field rotated in plane and out of plane (perpendicular) of S/F interfaces, respectively.

sented in Figs. 3(c) for field rotated in plane and 3(d) for a field rotated out of plane. We found that above 3 KG pronounced anisotropy arises in the field-angle-dependent resistance. The anisotropy gets stronger with increasing magnetic field strength. The anisotropy can be explained if we consider the microconstriction to have the shape of a nanowire and the field is rotated with respect to the direction of flow of the current through this wire. This kind of angular magnetoresistance (AMR) is usually seen in materials which have surface states with complex spin structure [30,31]. Such two-fold symmetry in AMR is also seen in materials with high spin-orbit coupling. Hence, as far as spin-resolved PCAR experiments are concerned, $\text{Co}_3\text{Sn}_2\text{S}_2$ is not a half metal and the measured value of spin polarization is far less than 100%.

IV. BANDSTRUCTURE CALCULATION & ANALYSIS

It is imperative to understand the possible mechanism that leads to the reduction of spin polarization (spin “depolarization”). To gain understanding on that, we performed electronic structure calculations in the ferromagnetic phase of $\text{Co}_3\text{Sn}_2\text{S}_2$. The *ab initio* calculation was done using the Vienna *ab initio* Simulation Package (VASP) [32,33,36–38]. The space-group symmetry of $\text{Co}_3\text{Sn}_2\text{S}_2$ is $R\bar{3}m(166)$ and can be represented in a hexagonal [34] or a rhombohedral representation [1,2,5] where we used the first one. We used the experimentally obtained lattice parameters [35]. We found a ferromagnetic ground state with the magnetic moment of 0.35 and 0.34 μ_B/Co [without and with spin-orbit coupling (SOC)], respectively. Our density functional theory (DFT) values of magnetization agrees well with prior DFT calculations [1,2,34] and are also in good agreement with the experimental values of 0.29–0.33 μ_B/Co . Here it should be noted that though the Fermi level spin polarization was dramatically suppressed due to SOC, the magnetization with SOC did not get altered noticeably. This is because the

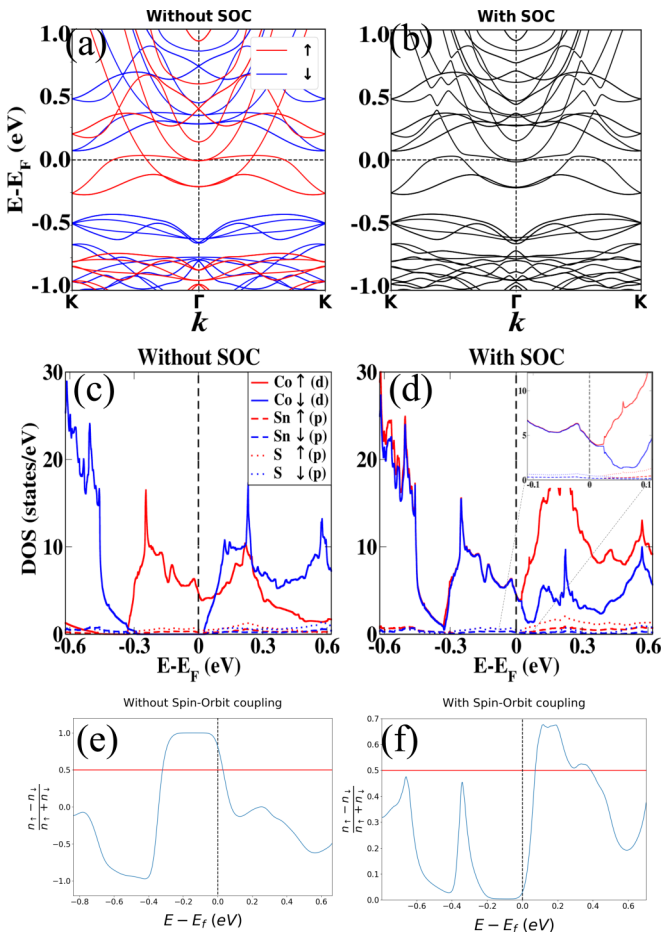


FIG. 4. (a),(b) Computed band structures are shown for calculations without and with SOC, respectively. In (a), red and blue color lines represent spin-up and spin-down states, respectively, while in (b) such spin-resolved bands become indistinguishable due to SOC. The band structures are consistent with the previous calculations [34]. (c),(d) Corresponding DOS for the above two cases, respectively. For DOS, we project the total DOS into different orbitals and spin states for both without and with SOC. The most distinguishing feature of the result is that with SOC, the DOS for spin-up and spin-down states overlap for an energy span of 250-meV below the Fermi level, despite the magnetization remaining comparable to that without SOC. Inset: Inset figure in (d) zooms out the low-energy region. (e),(f) Computed spin polarization curves without SOC and with SOC, respectively.

calculation of the magnetic moment involves averaging over all the filled bands. On the other hand, for transport spin polarization, only the bands crossing the Fermi surface contribute [15,34]. We present the calculated band structures and the corresponding density of states (DOS) in Figs. 4(a) and 4(c). Here, we find a large spin splitting of the band structure as well as in the DOS. In this case, it is possible to separate the bands for the two spin states since spin is a good quantum number [Fig. 4(a)].

In Fig. 4(e) we present the computed curve for degree of spin polarization. Here, it is clearly seen that the system is 100% spin polarized at the Fermi level. A lower spin polarization could result due to charge doping, which might cause a shift in chemical potential. If the shift is about 50 meV,

then the spin polarization is equal to 50%, the maximum value measured in our experiments. To have even lower spin polarization the chemical potential must shift further and the spin polarization can be completely suppressed for a shift of 100 meV. We indeed measured extremely low values of spin polarization at several points. However, compositional analysis of the crystals did not reveal noticeable deviations from desired stoichiometry at different points that could explain such a shift. Furthermore, since defects are distributed randomly over the sample, statistically speaking, at least some of the points on which PCAR was performed should have shown a spin polarization of 100% if suppression was due to charge doping alone. This warrants the search for an intrinsic source of spin depolarization in $\text{Co}_3\text{Sn}_2\text{S}_2$.

Spin-orbit coupling is an important intrinsic mechanism that might play a role here. Thus, we performed band-structure calculations including the role of spin-orbit coupling (see Fig. 4) for $\text{Co}_3\text{Sn}_2\text{S}_2$. In this case, the band structure [Fig. 4(b)] shows similar dispersion features as in the case without the SOC [Fig. 4(a)]. However, since spin is no longer a good quantum number here, spin-resolved bands cannot be extracted. The band structure and the value of the magnetic moment calculated while including SOC agrees well with the previous DFT calculations [34]. We plotted the DOS projected on each of the spin states, as well as on different orbitals as shown in Figs. 4(c) and 4(d). As expected, the low-energy states are dominated by the Co- d orbitals. Although the SOC strength of the Co- d is often expected to be less, here due to the presence of Sn and S cations and owing to the loss of time-reversal symmetry in the ferromagnetic state, the spin-orbit splitting is enhanced. While the DOS plot without SOC revealed only one spin species is getting populated at the Fermi level [Fig. 4(c)] surprisingly DOS calculated with SOC shows that at the Fermi surface the opposite spin species get equally populated [Fig. 4(d)] making the spin polarization zero [Fig. 4(f)]. In this case, a very small shift in chemical potential, of the order of a few meV, could result in the detection of spin polarization values much lower than 100%, which agrees well with our experimental results. Additionally, calculations with SOC reveal that, while the DOS itself is slightly particle-hole asymmetric, the spin-polarization has, to a great extent, lost this symmetry. This delineates the source of particle-hole asymmetry as observed in the experimentally obtained Andreev reflection spectra.

V. CONCLUSIONS

In conclusion, from spin-polarized Andreev reflection spectroscopy on the ferromagnetic Weyl semimetal $\text{Co}_3\text{Sn}_2\text{S}_2$ we show that the transport spin polarization in the system is far less than what is expected for a half metal. In addition, the Andreev reflection spectra are reproducibly asymmetric regardless of the barrier strength. Our calculations reveal that both the key observations, namely the spin depolarization and the anisotropic Andreev reflection spectra, are primarily consequences of spin-orbit coupling. Given that, in spite of a spin-depolarization effect in the low-energy states below the Fermi level, the magnetic moment is large in this system, we may conclude that the magnetic moment comes from the electrons lying at a higher binding energy and thus the magnetization is local in nature.

ACKNOWLEDGMENTS

R.K. acknowledges CSIR, India for senior research fellowship. G.S. acknowledges financial support from a SERB extramural grant (Grant No. EMR/2016/003998) and a Swar-

najayanti fellowship awarded by the Department of Science and Technology (DST), Govt. of India under Grant No. DST/SJF/PSA-01/2015-2016.

- [1] E. Liu, Y. Sun, N. Kumar, L. Muechler, A. Sun, L. Jiao, S.-Y. Yang, D. Liu, A. Liang, Q. Xu, J. Kroder, V. Süß, H. Borrmann, C. Shekhar, Z. Wang, C. Xi, W. Wang, W. Schnelle, S. Wirth, Y. Chen, S. T. B. Goennenwein, and C. Felser, *Nat. Phys.* **14**, 1125 (2018).
- [2] Q. Wang, Y. Xu, R. Lou, Z. Liu, M. Li, Y. Huang, D. Shen, H. Weng, S. Wang, and H. Lei, *Nat. Commun.* **9**, 3681 (2018).
- [3] W. Schnelle, A. Leithe-Jasper, H. Rosner, F. M. Schappacher, R. Pottgen, F. Pielhofer, and R. Wehrich, *Phys. Rev. B* **88**, 144404 (2013).
- [4] M. Holder, Y. S. Dedkov, A. Kade, H. Rosner, W. Schnelle, A. Leithe-Jasper, R. Wehrich, and S. L. Molodtsov, *Phys. Rev. B* **79**, 205116 (2009).
- [5] Q. Xu, E. Liu, W. Shi, L. Muechler, J. Gayles, C. Felser and Y. Sun, *Phys. Rev. B* **97**, 235416 (2018).
- [6] H. Yang, W. You, J. Wang, J. Huang, C. Xi, C. Cao, M. Tian, Z.-A. Xu, J. Dai, and Y. Li, *Phys. Rev. Mater.* **4**, 024202 (2020).
- [7] Y. Lu, N. Jia, L. Su, C. Owens, G. Juzeliūnas, D. I. Schuster, and J. Simon, *Phys. Rev. B* **99**, 020302(R) (2019).
- [8] F. D. M. Haldane, *Phys. Rev. Lett.* **93**, 206602 (2004).
- [9] S. K. Upadhyay, A. Palanisami, R. N. Louie, and R. A. Buhrman, *Phys. Rev. Lett.* **81**, 3247 (1998).
- [10] N. Auth, G. Jakob, T. Block, and C. Felser, *Phys. Rev. B* **68**, 024403 (2003).
- [11] S. Kamboj, S. Das, A. Sirohi, R. R. Chowdhury, S. Gayen, V. K. Maurya, S. Patnaik, and G. Sheet, *J. Phys.: Condens. Matter* **30**, 355001 (2018).
- [12] L. Aggarwal, S. Gayen, S. Das, R. Kumar, V. Su, C. Felser, C. Shekhar, and G. Sheet, *Nat. Commun.* **8**, 13974 (2016).
- [13] A. Sirohi, C. K. Singh, G. S. Thakur, P. Saha, S. Gayen, A. Gaurav, S. Jyotsna, Z. Haque, L. C. Gupta, M. Kabir, A. K. Ganguli, and G. Sheet, *App. Phys. Lett.* **108**, 242411 (2016).
- [14] S. Mukhopadhyay, P. Raychaudhuri, D. A. Joshi, and C. V. Tomy, *Phys. Rev. B* **75**, 014504 (2007).
- [15] P. Vaquero and G. G. Sobany, *Solid State Sci.* **11**, 513 (2009).
- [16] See Supplemental Material at <http://link.aps.org/supplemental/10.1103/PhysRevB.102.104434> for more details on sample preparation, experimental technique, and additional data.
- [17] A. M. Duif, A. G. M. Jansen, and P. Wyder, *J. Phys.: Condens. Matter* **1**, 3157 (1989).
- [18] G. Sheet, S. Mukhopadhyay, and P. Raychaudhuri, *Phys. Rev. B* **69**, 134507 (2004).
- [19] A. G. M. Jansen, A. P. van Gelder, and P. Wyder, *J. Phys. C: Solid State Phys.* **13**, 6073 (1980).
- [20] G. E. Blonder, M. Tinkham, and T. M. Klapwijk, *Phys. Rev. B* **25**, 4515 (1982).
- [21] G. J. Strijkers, Y. Ji, F. Y. Yang, C. L. Chien, and J. M. Byers, *Phys. Rev. B* **63**, 104510 (2001).
- [22] R. J. Soulen, Jr., M. S. Osofsky, B. Nadgorny, T. Ambrose, P. Broussard, and S. F. Cheng, *J. Appl. Phys.* **85**, 4589 (1999).
- [23] I. I. Mazin, *Phys. Rev. Lett.* **83**, 1427 (1999).
- [24] P. Chalsani, S. K. Upadhyay, O. Ozatay, and R. A. Buhrman, *Phys. Rev. B* **75**, 094417 (2007).
- [25] Y. Miura, K. Nagao, and M. Shirai, *Phys. Rev. B* **69**, 144413 (2004).
- [26] M. Mehta, G. Sheet, D. A. Dikin, S. Lee, C. W. Bark, J. Jiang, J. D. Weiss, E. E. Hellstrom, M. S. Rzczowski, C. B. Eom, and V. Chandrasekhar, *Appl. Phys. Lett.* **97**, 012503 (2010).
- [27] R. F. Gasperovic, B. N. Taylor, and R. E. Eck, *Solid State Commun.* **4**, 59 (1966).
- [28] J. Bardeen, L. N. Cooper, and J. R. Schrieffer, *Phys. Rev.* **108**, 1175 (1957).
- [29] To note, there is no physical reason why the extrapolation has to be linear, but that is what is typically done in modified BTK analysis. Nevertheless, the main result—namely the observation of nonhalf metallicity—is not altered by this.
- [30] T. Shang, Q. F. Zhan, L. Ma, H. L. Yang, Z. H. Zuo, Y. L. Xie, H. H. Li, L. P. Liu, B. M. Wang, Y. H. Wu, S. Zhang, and R. W. Li, *Sci. Rep.* **5**, 17734 (2015).
- [31] A. Kandala, A. Richardella, S. Kempinger, C. X. Liu, and N. Samarth, *Nat. Commun.* **6**, 7434 (2015).
- [32] G. Kresse and J. Furthmüller, *Phys. Rev. B* **54**, 11169 (1996).
- [33] To describe the core electrons we used projector augmented wave (PAW) [38] pseudopotentials and for the exchange-correlation functional we used the Perdew-Burke-Ernzerhof (PBE) [37] form. The cutoff energy for the plane wave basis was set to 500 eV. The Monkhorst-Pack k -mesh was set to $15 \times 15 \times 6$ in the Brillouin zone for the self-consistent calculation.
- [34] J.-X. Yin, S. S. Zhang, G. Chang, Q. Wang, S. S. Tsirkin, Z. Guguchia, B. Lian, H. Zhou, K. Jiang, I. Belopolski, N. Shumiya, D. Multer, M. Litskevich, T. A. Cochran, H. Lin, Z. Wang, T. Neupert, S. Jia, H. Lei, and M. Z. Hasan, *Nat. Phys.* **15**, 443 (2019).
- [35] The experimental lattice parameters are $a = 5.38 \text{ \AA}$, $b = 5.38 \text{ \AA}$, $c = 13.19 \text{ \AA}$ [36], and $\alpha = \beta = 90^\circ$, $\gamma = 120^\circ$.
- [36] S. P. Ong, W. D. Richards, A. Jain, G. Hautier, M. Kocher, S. Cholia, D. Gunter, V. L. Chevrier, K. A. Persson, and G. Ceder, *Comput. Mater. Sci.* **68**, 314 (2013).
- [37] John P. Perdew and K. Burke, Kieron and M. Ernzerhof, *Phys. Rev. Lett.* **77**, 3865 (1996).
- [38] M. B. Mineev-Weinstein and S. P. Dawson, *Phys. Rev. E* **50**, R24(R) (1994).